JGR Space Physics

METHOD

10.1029/2024JA032925

GOES-R Series X-Ray Sensor (XRS): 1. Design and Pre-Flight Calibration

Thomas N. Woods[1], Thomas Eden[1], Francis G. Eparvier[1], Andrew R. Jones[1], Donald L. Woodraska[1], Phillip C. Chamberlin[1], and Janet L. Machol[2,3]

[1]Laboratory for Atmospheric and Space Physics, University of Colorado, Boulder, CO, USA, [2]Cooperative Institute for Research in Environmental Sciences, University of Colorado, Boulder, CO, USA, [3]NOAA National Centers for Environmental Information, Boulder, CO, USA

Key Points:

- New technology for the Geostationary Operational Environmental Satellites (GOES) X-Ray Sensor (XRS) is now continuing the five-decade record of solar X-ray flare monitoring
- NOAA measurement requirements for XRS led to a new design of the XRS with four photometers to measure the two standard X-ray bands
- This new XRS instrument has improved pre-flight calibrations and a new capability to provide real-time the location of flares on the Sun

Correspondence to:

T. N. Woods,
tom.woods@lasp.colorado.edu

Citation:

Woods, T. N., Eden, T., Eparvier, F. G., Jones, A. R., Woodraska, D. L., Chamberlin, P. C., & Machol, J. L. (2024). GOES-R Series X-Ray Sensor (XRS): 1. Design and pre-flight calibration. *Journal of Geophysical Research: Space Physics*, *129*, e2024JA032925. https://doi.org/10.1029/2024JA032925

Received 29 MAY 2024
Accepted 12 NOV 2024

Author Contributions:

Conceptualization: Thomas N. Woods, Francis G. Eparvier, Andrew R. Jones, Phillip C. Chamberlin
Formal analysis: Thomas Eden, Janet L. Machol
Funding acquisition: Thomas N. Woods, Francis G. Eparvier
Project administration: Francis G. Eparvier
Software: Donald L. Woodraska
Writing – original draft: Thomas N. Woods
Writing – review & editing: Thomas Eden, Francis G. Eparvier, Andrew R. Jones, Donald L. Woodraska, Phillip C. Chamberlin, Janet L. Machol

Abstract The X-Ray Sensor (XRS) has been making full-disk observations of the solar soft X-ray irradiance onboard National Oceanic and Atmospheric Administration's (NOAA) Geostationary Operational Environmental Satellites since 1975. Critical information about solar activity for space weather operations is provided by XRS measurements, such as the classification of solar flare magnitude based on X-ray irradiance level. The GOES-R series of XRS sensors, with the first in the series launched in November 2016, has a completely different instrument design compared to its predecessors, GOES-1 through GOES-15. To provide continuity, the two GOES-R XRS spectral bands remain unchanged providing the solar X-ray irradiance in the 0.05–0.4 nm and 0.1–0.8 nm bands. The changes for the GOES-R XRS instrument included using Si photodiodes instead of ionization cells to improve performance, using multiple channels per X-ray band to allow for a wider dynamic range, and providing accurate radiometric calibrations using the National Institute of Standards and Technology (NIST) Synchrotron Ultraviolet Radiation Facility in Gaithersburg, Maryland. In addition to the standard XRS data product of solar irradiances in the two X-ray bands, a new real-time flare location data product is also available from the GOES-R XRS instruments because two channels are quadrant photodiodes for position detection. The design and pre-flight calibration results for this next-generation XRS instrument are presented here in this XRS Paper-1, and in-flight solar X-ray measurements from GOES-16, GOES-17, and GOES-18 are provided in the XRS Paper-2.

1. Introduction

Geostationary Operational Environmental Satellites (GOES) have been observing the terrestrial weather since 1975, as well as monitoring space weather that includes observing solar flares, solar eruptive events, and the space environment (fields and particles) in-situ at the GOES satellites in geostationary orbit. The GOES space weather observations are critical for making accurate space weather forecasts concerning how the Sun, both particles and photons, affects the terrestrial space environment and our space-based technology assets, such as satellites, communication systems, and navigation systems. The National Oceanic and Atmospheric Administration (NOAA) requirements for GOES space weather observations include two identical operational GOES satellites in geostationary orbit, with one near the east coast (longitude 75.2° west) and one near the west coast (longitude 137.2° west) for full surface weather coverage of the United States and for redundancy of space weather measurements. NOAA also maintains at least one additional GOES satellite as an on-orbit backup (storage). The GOES-R series include four satellites (GOES-R, GOES-S, GOES-T, and GOES-U). These satellites were launched on 19 November 2016, 1 March 2018, 1 March 2022, and 25 June 2024, respectively, and after which they were renamed GOES-16, 17, 18, and 19, respectively. GOES-16 and GOES-18 are the primary operational satellites now. GOES-17 is currently in storage, and GOES-16 is expected to go into storage after GOES-19 is fully commissioned.

There is a long and continuous record of monitoring for solar X-ray flares from the GOES satellite series, starting with the first GOES satellite in 1975. These data from the X-Ray Sensor (XRS) provide the primary measurements used to classify the magnitude and duration of solar X-ray flares. XRS is designed to measure the full-disk solar X-ray irradiance in two broadband wavelength intervals: (a) $\Delta\lambda = 0.05$–0.4 nm, called XRS-A (also known as the XRS "short" channel); (b) $\Delta\lambda = 0.1$–0.8 nm, called XRS-B (XRS "long" channel). Both intervals are in the soft X-ray (SXR) range that extends between 0.1 and 10 nm.

The X-ray flare classification is based on the XRS-B 1-min-averaged peak intensity for a flare. The X-ray flare classification includes a letter (A, B, C, M, and X) that represents an order of magnitude of XRS-B irradiance and

a number (1–9) within the specified order. For example, an X5 flare has a peak irradiance of 5×10^{-4} W m^{-2}; whereas, a M5 flare has 10 times lower irradiance. If the flare is larger than 10^{-3} W m^{-2}, then the number is extended beyond 9. For example, an X12 flare has a peak irradiance of 12×10^{-4} W m^{-2}. The flare classification is based on the irradiance truncated to one decimal place.

For more accurate solar X-ray irradiance values, the NOAA Space Weather Prediction Center (SWPC) recommends scaling of the previous XRS reported values for GOES-15 and earlier satellites. Their recommended scaling is that the XRS-B band reported values need to be multiplied by 1.43 (divided by 0.70) to convert from flare levels (e.g., C, M, X) to physical irradiance units of W m^{-2}. This correction was confirmed for GOES-15 XRS-B using SXR spectra from the Miniature X-ray Solar Spectrometer (MinXSS) CubeSat as described by Woods et al. (2017). Similarly, NOAA SWPC recommends that the earlier XRS-A reported values need to be multiplied by 1.18 (divided by 0.85) to convert to physical irradiance units of W m^{-2}. As of September 2024, the corrections have been applied to the reprocessed science-quality data for GOES-8 through −15 and will be applied to earlier satellites later in 2024. For more information on the previous XRS calibration, see: https://www.ncei.noaa.gov/data/goes-space-environment-monitor/access/science/xrs/GOES_1-15_XRS_Science-Quality_Data_Readme.pdf.

The combination of the XRS-A and B data is commonly used to provide an estimate of the coronal plasma temperature. One technique to estimate the corona temperature is to relate the ratio of the XRS-A irradiance to the XRS-B irradiance using a spectral model for the solar irradiance (Garcia, 1994; White et al., 2005; Woods et al., 2023). This simple ratio of XRS-A irradiance to XRS-B irradiance is routinely used real-time by space weather operators to forecast the end of the flare rise period because the corona flare temperature usually peaks right before the X-ray irradiance peaks (Hudson, 2011). The soft X-ray (SXR) flare rise period is also known as the flare impulsive phase when hard X-ray (HXR) and many extreme ultraviolet (EUV) emissions usually peak prior to the flare thermal gradual phase when the SXR emissions peak. The impulsive phase and gradual phase energetics are related through the Neupert effect (Neupert, 2011) where the integration of the impulsive phase HXR irradiance is an estimate of the gradual phase SXR energy. Similarly, one can use the inverse Neupert effect by taking the derivative of the gradual phase SXR irradiance to estimate the impulsive phase HXR profile.

The XRS real-time data are also routinely used by space weather operators to forecast radio blackouts and solar energetic particle (SEP) events (see https://www.swpc.noaa.gov/noaa-scales-explanation for the NOAA space weather scale definitions). The radio blackouts are forecast whenever the XRS-B irradiance is higher than a M1 flare level. It is important to forecast the SEP events because they pose a serious threat to the safety of our space-based technology assets, and also radiation safety concerns for astronauts, who would need to seek shelter during SEP events. Because the solar X-ray photons travel at the speed of light and arrive at Earth in about 8 min, the slower moving energetic particles from an eruptive flare event will arrive at Earth at a later time. A SEP event is forecasted based on the XRS-B irradiance level and flare location. The solar radiation storm scale is measured for SEP events impacting Earth by in-situ particle flux measurements on GOES satellites for particles that have kinetic energies greater than 10 MeV. In addition, coronal mass ejection (CME) events are often associated with eruptive flares, and the CME impacts on Earth are measured by the geomagnetic k_p index. Studies of the statistical relationship between CMEs and flare magnitude indicate that there are CMEs for ∼20% of C-class flares, ∼50% for M-class flares, and ∼100% for X-class flares (Hudson, 2011; Wang & Zhang, 2007; Woods et al., 2011).

The version of XRS that was used through GOES-15 consists of two ionization cells for the two different XRS bands (e.g., Garcia, 1994). The sensor electronics for these ion-cell XRS sensors had dynamic range limitations for both the low and high end of its measurement range. Near the lower limit, irradiance measurements on the previous XRS sensors would drop to noise levels ("bottom out"), which prevented any true measure of a solar-minimum irradiance level (e.g., Woods et al., 2017). For the upper-level limit, all previous XRS sensors could not measure flare levels above about X24 (with calibration scaling applied) due to sensor electrometer saturation limit. This high limit was surpassed by 12 events between 1978 and 2003 (Hudson et al., 2024), including during the extreme flares that occurred on 28 October 2003 and 4 November 2003.

Another limitation with the previous XRS sensors is related to the accuracy of the measurements based on the limited pre-flight radiometric calibrations that were performed, and the inability to directly monitor for long-term degradation of the XRS channels. The irradiance accuracy is important for comparing data from different in-

Table 1
Key Requirements and Performances for GOES-R X-Ray Sensor

	XRS-A channel		XRS-B channel	
Parameter	Requirement	Performance	Requirement	Performance
Spectral Range (nm)	0.05–0.4	0.09–0.37	0.1–0.8	0.10–0.69
Out-of-Band Rejection (%)	<10%	2.8%	<10%	6.3%
Irradiance Range (W m^{-2})	10^{-9} to 10^{-3}	10^{-9} to 10^{-2}	10^{-8} – 4×10^{-3}	10^{-9} to 10^{-2}
Resolution (3-s, W m^{-2})	$<2 \times 10^{-10}$	3.0×10^{-10}	$<2 \times 10^{-9}$	2.5×10^{-10}
Precision (3-s, W m^{-2})	$<1.4 \times 10^{-8}$	3.8×10^{-9}	$<1.4 \times 10^{-7}$	3.8×10^{-9}
Irradiance Accuracy (%)	<20%	10%	<20%	10%
Spatial Coverage (FOV, arcmin)	>±20	±70	>±20	±70

Note. See the text in Section 2 about the details of these XRS requirements and performances.

family XRS sensors, or for making comparisons over long periods of time with the same instrument. NOAA has fortunately been able to have overlapping XRS measurements since the 1970s to maintain a consistent solar SXR record by being able to adjust new XRS measurements to the other operating XRS instruments. Comparisons of overlapping XRS measurements and other solar X-ray irradiance measurements have led to the recommended scaling of XRS reported irradiance values on the older XRS instruments as noted earlier. While there has not been any noticeable XRS sensitivity degradation for the earlier missions, the XRS background levels and temperature-dependent gain corrections have changed over time, and those time-dependent corrections have been incorporated into the latest reprocessing of all prior GOES XRS data.

These limitations for the previous XRS instruments have largely been resolved with a new design for the XRS sensors as part of the GOES-R Extreme-ultraviolet and X-ray Irradiance Sensors (EXIS) system. Chamberlin et al. (2009) describe in detail the new GOES-R XRS design and the motivation for those changes. The key changes for the new XRS design are also summarized here. The primary change is the use of stable Si photodiodes (Korde & Canfield, 1989) instead of ion-cells. The new-generation XRS units continue to use Be foil filters for limiting the passbands in the X-ray range, as was done for the previous XRS units. There are two decades of heritage for using Si photodiodes to measure the solar SXR irradiance from the X-Ray Photometer System (XPS) that is part of the Solar EUV Experiment (SEE) (Woods, Eparvier, et al., 2005) onboard the Thermosphere Ionosphere Mesosphere Energetics and Dynamics (TIMED) satellite, as well as similar XPS sensors that have flown on the Student Nitric Oxide Experiment (SNOE) (Bailey et al., 2000) and the SOlar Radiation and Climate Experiment (SORCE) (Woods, Rottman, & Vest, 2005). The other primary change for the new XRS is the use of multiple channels for each of the XRS bands (A and B) to expand the measurement dynamic range. In addition, two of those extra channels are quadrant photodiodes that enable detection of flare location, and the new XRS data product of flare location compliments the GOES solar EUV imager observations of flares. There was another 5 years of XRS development after the Chamberlin et al., 2009 paper was written, so this paper, XRS Paper-1, documents the final (as-flown) design for the GOES-R XRS, as well as, provides results about the pre-flight calibrations for the XRS instruments and some of the early-orbit performance results during the EXIS commissioning phase. We note that all four GOES-R satellites are already in space, and that more detailed in-flight performance results for these XRS instruments are presented in the XRS Paper-2 by Machol et al. (2024).

2. XRS Instrument Overview

The GOES-R series of XRS instruments have the basic goal of continuing the almost five decades of solar soft X-ray measurements from previous XRS instruments. The key XRS requirements, as listed in Table 1, are specified in NOAA's Performance and Operational Requirements Document (PORD; not publicly available) for the GOES-R EXIS instrument, and those requirements have guided the design choices for the new XRS instrument design. For example, two photodiodes with different aperture areas were chosen to address the requirement to measure the solar X-ray irradiance over more than six orders of magnitude and the requirement to have a signal-to-noise ratio (SNR) greater than one for 10-min averages (see Table 1). We refer to the four channels in the GOES-R Series XRS as XRS-A1 and XRS-A2 for the A band, and XRS-B1 and XRS-B2 for the B band. The A1 and B1 channels

Table 2
GOES-R X-Ray Sensor (XRS) Design Specifications

Parameter	XRS-A1	XRS-A2	XRS-B1	XRS-B2
Description	A MIN	A MAX/FLARE	B MIN	B MAX/FLARE
Spectral Range	0.05–0.4 nm	0.05–0.4 nm	0.1–0.8 nm	0.1–0.8 nm
Si Diode Type	AXUV100	AXUVPS6 Quad	AXUV100	AXUVPS6 Quad
Si Diode Active Area	10 mm × 10 mm	7.6 mm Dia.	10 mm × 10 mm	7.6 mm Dia.
Aperture Size	9 mm × 9 mm	2.1 mm × 2.1 mm	9 mm × 9 mm	2.1 mm × 2.1 mm
Si Diode Thickness	50 μm	50 μm	50 μm	50 μm
Be Filter Thickness	600 μm	600 μm	60 μm	60 μm
Model Signal	32 fA–32 nA	1.6 fA–1.6 nA	110 fA–44 nA	6 fA–2 nA

Note. Model Signal values that are outside the ASIC electrometer range (6 fA–6 nA) are underlined. Two channels are used for each passband to cover full range of solar activity.

are designed to make measurements near solar cycle minimum, and thus have a larger aperture area of 81.0 mm^2. This is the maximum aperture area achievable given the constraints of both the Si photodiode detector size and the field-of-view (FOV) requirement. The A2 and B2 channels are designed to measure the solar flares and thus have smaller aperture area of 4.5 mm^2. The new XRS B2 design is expected to be able to measure up to about X120 flare level before saturation. The A2 and B2 detectors are quadrant photodiodes (OptoDiode AXUV-PS6) instead of single element photodiodes (OptoDiode AXUV-100) as used for A1 and B1. The capability of A2 and B2 channels to determine the location of solar flares is described later in Section 4. As an end data product, the XRS A and B band irradiances are reported as single values with the irradiance values selected from the optimum photodiode based on a predefined irradiance level, as discussed more by Machol et al. (2024). The choice to have two photometers with different aperture sizes for each XRS band provides some redundancies, plus the EXIS electronics have fully redundant interface electronics to the XRS instrument, referred to as the EXIS A-side (primary-side) and B-side (secondary-side) electronics.

In Table 1, the listed values for the requirements are the values provided in the XRS PORD, and the listed values for the performances are from pre-flight calibrations and/or in-flight measurements. The performance for Spectral Range is based on calculating the signal as a function of wavelength using the pre-flight responsivity and a flat spectrum and then identifying the wavelength range that contains 90% of the total signal. Out-of-Band Rejection performance values are calculated with the XRS signal model over the required spectral range. Irradiance Resolution is defined as 1 Data Number (DN) for the diode electrometer, and Precision is defined as the measurement precision that includes both electrometer noise and measurement statistics of the signal (e.g., standard deviation). Both the Irradiance Resolution and Precision are dependent on integration time, which is specified in the XRS PORD as 3 s. While those values listed in Table 1 are for 3-s measurements (averages), the XRS measurements are made with 1 s cadence on-orbit. Performance for Irradiance Range minimum value is 0.22 times the Precision performance value to account for 1-min averages. The performance for Irradiance Range maximum value is 5×10^7 times the Resolution performance value to account for the diode electrometer full range. The performance of the Irradiance Accuracy is calculated as the total uncertainty of the estimated irradiance at a C1 level using all of the pre-flight calibrations uncertainties (as discussed more in Section 4). XRS does not image the Sun, and thus the Spatial Coverage is the XRS FOV range as determined by the aperture and baffle design for the XRS photometers.

The choice for the thickness of the Be foil filters is the main design option to match the spectral passbands of XRS-A (0.05–0.4 nm) and XRS-B (0.1–0.8 nm). In addition, the thickness of the Si active layer impacts the short wavelength cutoff. The OptoDiode AXUV photodiodes chosen for flight have a Si thickness of 50 μm, which results in a short wavelength cutoff of about 0.05 nm. The new XRS design specifications, including the photodiode and Be filter specifications, are provided in Table 2, and the spectral responsivity for GOES-16 XRS is discussed in more detail in Section 3.

The XRS performance exceeds the requirements except for the spectral ranges and for the irradiance resolution for XRS-A. The lower value of the spectral range is determined primarily by the Si thickness for the photodiode.

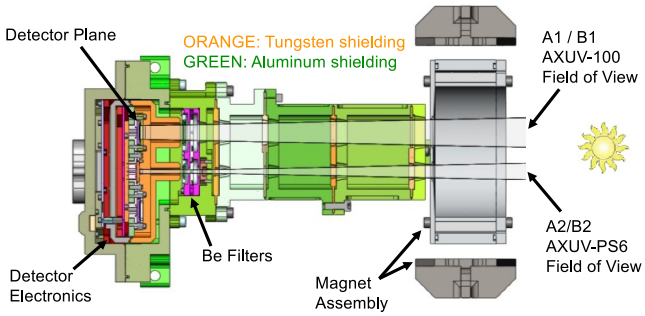

Figure 1. A cutout slice of the Geostationary Operational Environmental Satellites XRS instrument showing the low-Z Al housing (green) on the outside of the optical cavity and the high-Z W/Cu alloy (orange) that provides the inner walls. The Be filters, photodiodes, detector electronics, field-of-view baffles/collimator, and the magnet assembly (gray) are also shown.

OptoDiode was not successful in making photodiodes with 100 μm Si thickness as needed for the XRS-A channels, so the OptoDiode photodiodes with 50 μm Si thickness were flown for both XRS-A and XRS-B. Thus, the lower limit for the XRS-A spectral range is 0.09 nm due to the limitation of the Si thickness for the photodiodes and because of the very low solar spectral irradiance levels at the shorter wavelengths. The higher value of the spectral range performance is highly dependent on the solar spectrum used for the signal estimate, as discussed more in Section 3. There is a balance in designing the XRS electrometer to having low enough gain to meet irradiance resolution requirement and having high enough gain to meet irradiance range requirement. Those XRS-B requirements are less demanding than the XRS-A requirements, and thus it was feasible to meet all of the XRS-B requirements but not technically feasible to meet all of the XRS-A requirements. As the low solar cycle minimum irradiance levels are not important for space weather operations, the XRS-A electrometer gain was selected to meet the XRS-A irradiance range requirement but to compromise slightly on the XRS-A irradiance resolution performance.

The XRS science FOV requirement is >±20 arcmin, but the implemented FOV is ±70 arcmin, or just over 2°. This larger FOV was needed to account for several driving requirements: ±27 arcmin for the diameter of the Sun at X-ray wavelengths, ±7 arcmin for accuracy of the spacecraft pointing toward the Sun, and ±25 arcmin for alignment of each channel boresight to the reference optical boresight of the pointing platform that XRS is mounted on, as well as internal alignment of all the optical components (photodiodes and apertures). The GOES-R XRS FOV design has ±11 arcmin of margin.

Another significant design driver is the shielding of the XRS optical cavity from the large number of energetic electrons that are present in the space environment at geostationary orbits. The shielding is needed to prevent most of these electrons from reaching the detectors and to also mitigate the Bremsstrahlung X-ray radiation emitted when these electrons interact with the XRS housing. The XRS radiation shielding has three components: (a) a thick, outer layer of low atomic number (low-Z) material, aluminum (Al), to essentially stop all off-axis energetic electrons; (b) an inner layer of high atomic number (high-Z) material, tungsten (W), to absorb the bremsstrahlung X-ray radiation that was created in the outer aluminum shield; and (c) a strong magnet assembly in front of XRS to sweep away electrons from the instrument boresight. Figure 1 shows the location of Al and W shielding and the magnet assembly in the new XRS optical design. Chamberlin et al. (2009) provide more details about the design analysis for the shielding. Briefly here, the XRS magnet was designed to have 800 G (0.08 Telsa) over a length of 5 cm in order to remove on-axis electrons up to an energy of 5 MeV, and Geant4 and MULASSIS models (Agostinelli et al., 2003; Lei et al., 2002) were performed during the development phase to determine an optimal Al thickness of 7 mm and optimal W thickness of 5 mm.

The electronics parts, including sensors, for XRS have extensive shielding as part of the design, and the parts were all radiation tested to verify that they could survive 15 years in geostationary orbit (one of the requirements in the EXIS PORD). These radiation tests included total integrated dose testing to 100 kRad and single event effects (SEE) testing with heavy ions. Because there is some degradation of the electrometer gain/offset as function of radiation dose, we did a pre-flight dose on all of the electrometers and sensors to effectively burn them in before launch so that the amount of in-flight degradation could potentially be at a lower rate. The electrometers have an internal gain-calibration mode (see Section 4.4) to help track any in-flight degradation of the electrometer electronics.

3. XRS Design Optimization

The XRS design requirements, with key requirements listed in Table 1, are specified by NOAA so that the GOES-R series XRS measurements can provide a time series that could be linked consistently to the past four decades of solar X-ray flare monitoring. To optimize the new XRS design, XRS signal models were developed and included the use of NOAA-specified reference solar spectra (minimum and maximum solar activity) with the XRS wavelength-dependent filter transmission function and detector sensitivities. The optimization of the filter

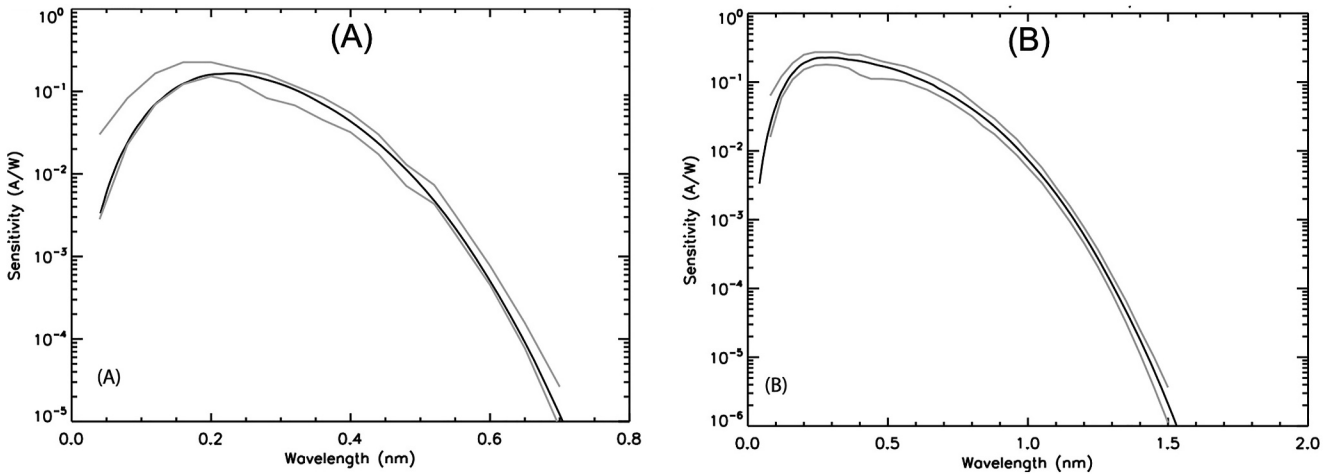

Figure 2. The PORD-required minimum and maximum spectral responsivity (gray) for XRS-A (left panel) and XRS-B (right panel) and the GOES-R XRS responsivity (black), showing the required spectral responsivity for each channel is met.

thickness (passband), signal range, and aperture area are briefly discussed in this section, and additional details about the GOES-R XRS design optimization are described by Chamberlin et al. (2009).

3.1. Passband Optimization

There are three design parameters to consider for the XRS passbands: choice of material for the X-ray filter, thickness of the filter, and thickness of the Si active layer. Be foil filters were selected to be the same filter material as used for previous XRS units, and the thickness of the Be foil defines the long-wavelength cutoff for the passband. The XRS responsivity model uses the Henke atomic constants database (Henke et al., 1993) to determine the spectral transmission of the Be filter and the Si detector. To match the required NOAA-specified XRS responsivity requirements, it was found that the Be filter thickness should be 600 μm for XRS-A and 60 μm for XRS-B. In order to mitigate the effect of a possible pinhole in these Be foil filters, two filters are used in series. Furthermore, the two-filter approach eliminates the large number of photoelectrons generated in the first filter from reaching the detector. The filters selected for the GOES-R series XRS are two 30-μm filters for the XRS-B channel; a 570-μm filter, along with a 30-μm filter for the XRS-A channel (with the 30-μm filter in front).

The Si active layer thickness defines the short-wavelength cutoff. From signal modeling, the optimal Si thickness was determined to be 100 μm for XRS-A and 50 μm for XRS-B. However, the 100 μm Si photodiodes were found to have a lower-than-desired shunt resistance, which causes an undesirable increase in detector noise. Therefore, 50 μm thick Si photodiodes were selected for both XRS-A and XRS-B.

Using those Be filter and Si photodiode parameters with atomic constants from Henke et al. (1993), the XRS responsivities are calculated and shown in Figure 2 along with a comparison to the NOAA requirements that are based on ionization cell versions of the earlier XRS instruments. As a reminder, the XRS-A band is 0.05–0.4 nm, and the XRS-B band is 0.1–0.8 nm. These XRS bands are not obvious from examining the responsivity curves in Figure 2 on a logarithm scale, so examining the XRS model signals, as shown in the next section, is important to verify the desired passband for the new XRS design.

3.2. XRS Signal Estimates

The XRS signal models are needed to verify that the appropriate electronics can be built to measure the expected signals with adequate margins on the signal-to-noise ratio at low solar activity and to not saturate for the largest possible flares. The XRS signal model is simply the XRS responsivity model (noted in previous section and in units of A/W) multiplied by a solar reference spectrum (units of W m^{-2} nm^{-1}) and also multiplied by the aperture area (units of m^2) to obtain the spectral signal distribution over wavelength, and this signal spectrum (units of A nm^{-1}) can then be integrated over all wavelengths to obtain the expected signal (units of A) for each XRS band. The NOAA-specified reference solar spectrum to use for signal model estimates is the Astrophysical Plasma Emission Code (APEC) (Smith et al., 2001). This model uses the Astrophysical Plasma Emission Database to

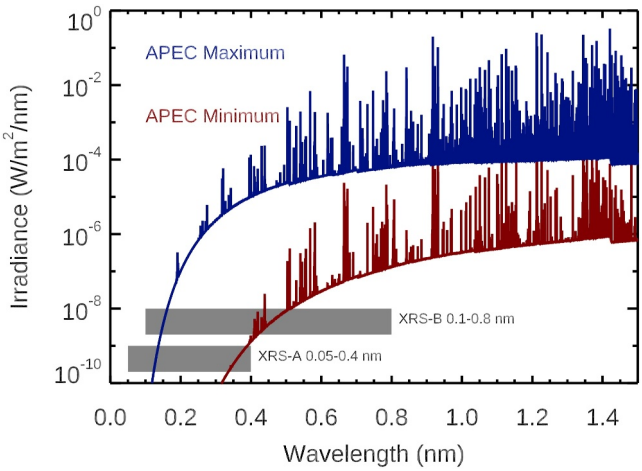

Figure 3. The Astrophysical Plasma Emission Code estimated solar irradiance at solar cycle maximum (blue) and minimum (red) conditions. The nominal passbands are also shown for XRS-A and XRS-B as the gray horizontal bars.

determine the spectral emissions of very hot plasmas. These reference model spectra, as specified by the XRS PORD, are adjusted in intensity so that the integrated irradiance of the APEC spectra over the XRS bands agree with the solar cycle minimum and maximum irradiance values provided in the XRS PORD. The APEC minimum (quiet) and maximum (active) solar spectra, as shown in Figure 3, include both the free-free continuum and bound-bound emissions associated with high-temperature plasma in solar corona. The estimated signal ranges for the XRS channels are listed in Table 2 for the minimum and maximum reference spectra.

This signal modeling also permits an examination of the passbands. By accumulating the signal from both the short wavelength and long wavelength, and normalizing to the total signal, the ideal passband is estimated for 90% of the model signal as shown in Figure 4. For example, the accumulated signal at 0.5 nm for each spectrum has two values, with one value from integrating the model signal from 0 nm up to 0.5 nm and second value from integrating from long wavelength (1.5 nm for the APEC spectra) down to 0.5 nm. Accumulating the signal in both wavelength directions helps to visual the spectral bands for different solar spectrum options. As expected, the ideal passband changes depending on the solar cycle condition (Quiet vs. Active), and these ideal passbands are skewed toward the high end of the required passbands (Spectral Range in Table 1) because the solar spectra are several orders of magnitude brighter in the 0.4–0.8 nm range than in the 0.01–0.2 nm range. A flat spectrum is also used in this analysis for defining the responsivity used in data processing and also to define the performance values for the spectral range and out-of-band rejection parameters listed in Table 1. Using the extremes for the quiet and active solar conditions, the actual solar passband for XRS-A is 0.26–0.60 nm, and solar passband for XRS-B is 0.45–1.12 nm. While these passbands extend to longer wavelengths than the required XRS passband requirements in Table 1, the center signal contributions (40%–60% of accumulated signal) do overlap with the high end of the required passbands. The XRS-A center passband is 0.37–0.50 nm, and XRS-B central passband is 0.67–0.92 nm. The design change to using Si photodiodes is not the cause for those differences in spectral ranges between solar spectra and flat spectrum, and such differences have existed on all previous versions of XRS with ion cells.

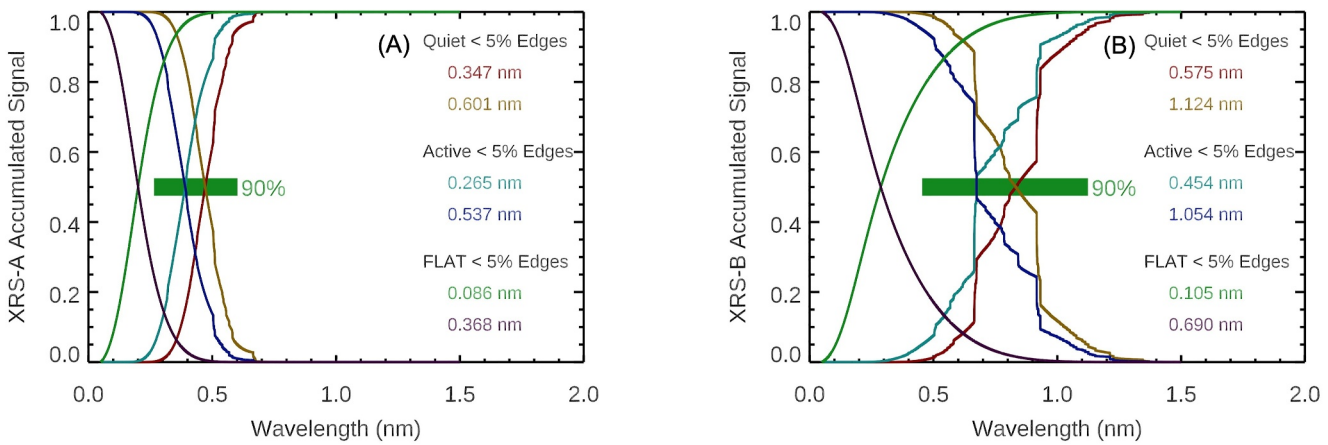

Figure 4. The modeled signals using the Astrophysical Plasma Emission Code Quiet and Active reference solar spectra and also a flat spectrum are accumulated from lower wavelength and from upper wavelength and normalized to the total signal to obtain the 5% edges to derive the ideal passband for 90% of the signal. The green, light-blue, and red lines are the model signals accumulated from lower wavelength for the Quiet spectrum, Active spectrum, and flat spectrum, respectively. The gold, dark-blue, and purple lines are the model signals accumulated from upper wavelength for the Quiet spectrum, Active spectrum, and flat spectrum, respectively. Left panel is for XRS-A, and right panel is for XRS-B. The thick green bar is the ideal passband for the solar signals.

3.3. Aperture Size Optimization

The aperture size can be optimized to scale the solar signal to be in the appropriate range for the detector electronics, namely the photodiode electrometers. The electrometer chosen for XRS is a specialized ASIC electrometer designed for GOES-R EXIS (Aalamia & Jones, 2009). This innovative low-noise, low-power electrometer design has six electrometer channels per IC and also has a gain calibration mode that permits tracking the gain changes for each electrometer channel over time. The charge resolution of this ASIC electrometer is set at 6 fC, so an integration time of 1 s corresponds to one output data number (DN) corresponding to a minimum current of 6 fA. However, the effective lower limit of the electrometer is driven by the internal electronics noise of about 10–20 fA $\times \sqrt{\text{Hz}}$. With this ASIC electrometer having a digital 20-bit counter output, the maximum current for measurements with 1-s integrations is 6 nA. As shown in Table 2, this electrometer, or any other viable commercial electrometer, cannot cover the full dynamic range of the solar X-ray variations, and hence, two channels with two different aperture areas are required for XRS observations.

As mentioned earlier, the XRS-A1 and XRS-B1 channels have a larger aperture (81 mm^2) for measurements during quiescent (non-flaring) solar activity, and the XRS-A2 and XRS-B2 channels have a smaller aperture (4.5 mm^2) for the flare measurements. The minimum channels (A1 and B1) are expected to determine the true solar cycle minimum level, unlike earlier versions of GOES XRS that bottomed out during solar cycle minimum (e.g., Woods et al., 2017). But these minimum channels (A1 and B1) are expected to saturate for large X-class flares. Whereas the maximum channels (A2 and B2) are expected to measure even the largest flares (at least up to X120) but will just measure electrometer noise during solar cycle minimum times. There is plenty of overlap, around three orders of magnitude, between the signals from the minimum and maximum channels, and the combination of both channels ensure that the entire solar X-ray irradiance range will be measured precisely. Chamberlin et al. (2009) provide more details about the choices for the aperture areas.

In reality, there is a stronger than expected response of the new XRS channels to the on-orbit energetic electrons for both the GOES-R XRS-A1 and XRS-B1 diodes, so the solar minimum levels continue to be a challenge for the X-ray bands. This effect of the on-orbit energetic electrons and in-flight performance of the XRS channels are discussed in more detail by Machol et al. (2024), but we note here that the smaller-aperture XRS-A2 and XRS-B2 are mostly impervious to on-orbit energetic electrons.

We note that the width and height of the individual apertures are precisely measured, and their nominal areas are calculated as the product of aperture width and height; however, the area values are not critical as long as the same area values are used in the Synchrotron Ultraviolet Radiation Facility (SURF) responsivity calculation and the solar irradiance calculation. In other words, the XRS responsivities, as discussed in Section 4.1, account for the aperture area.

3.4. Flare Location With Quadrant Photodiodes

It was realized early in the design of the XRS channels that the simple improvement of replacing a single photodiode with a quadrant photodiode (QD) would enable the new XRS instruments to provide valuable information about the location of the large flares on the solar disk. This flare location option with a quadrant photodiode is feasible because the flare, being a compact source on the Sun, has a significantly enhanced signal relative to the other quiescent (non-flare) radiation from the solar disk. This XRS detector enhancement can provide the flare location information near real-time for space weather operations with minimal amount of data processing, much less processing as needed for solar image processing to identify flare location. The details of the flare location algorithm for the XRS-A2 and B2 quadrant diodes are provided in XRS Paper-2 (Machol et al., 2024), along with in-flight performance of the flare position results and comparisons to flare locations determined by solar extreme ultraviolet imaging.

4. XRS Pre-Flight Calibrations

There are many XRS pre-flight tests and calibrations to verify that the XRS performance meets requirements, and the key test results for the responsivity, temperature-dependent background signal, temperature-dependent electrometer gain, FOV maps, and sensor linearity are discussed in this paper. The responsivity was determined for the previous GOES XRS instruments by modeling the responsivity of the ionization cell and adjusting the model to agree with calibration tests taken with a calibrated Fe^{55} gamma source with its primary emissions at

Table 3
GOES-R-Series X-Ray Sensor Calibration Results

GOES series	XRS-A1	XRS-A2	XRS-B1	XRS-B2
GOES-16	R 9.615×10^{-6}	R 5.064×10^{-7}	R 1.469×10^{-5}	R 7.768×10^{-7}
	T 516.6	T 524.0	T 53.4	T 53.2
GOES-17	R 9.577×10^{-6}	R 5.021×10^{-7}	R 1.479×10^{-5}	R 7.790×10^{-7}
	T 520.1	T 524.0	T 52.6	T 52.5
GOES-18	R 9.552×10^{-6}	R 5.111×10^{-7}	R 1.464×10^{-5}	R 7.982×10^{-7}
	T 522.0	T 519.3	T 53.8	T 52.7
GOES-19	R 9.670×10^{-6}	R 4.756×10^{-7}	R 1.432×10^{-5}	R 7.259×10^{-7}
	T 511.1	T 521.6	T 56.7	T 54.3

Note. Responsivity (R) is in units of Amps/(W/m^2). Modeled Be foil thickness (T) is in units of μm and has uncertainty of 0.3 and 0.1 μm for XRS-A and XRS-B, respectively. Initial R and T values were the average of results from using four different SURF beam energies. Some responsivity were revised post-launch. Values in table are current as of 20 September 2024.

5.90 keV (0.21 nm) and 6.49 keV (0.19 nm) (Hill et al., 2005). For the new GOES-R XRS instruments, more detailed calibrations were performed by using the National Institute of Standards and Technology (NIST) SURF in Gaithersburg, Maryland. In addition, the SURF facility and its calibration capabilities are used to perform FOV mapping of each XRS channel using a two-axis (pitch, yaw) gimbal system inside the SURF Beam Line 2 (BL2) vacuum tank and to provide validation of the XRS linearity by precisely changing the SURF beam intensity (e.g., Woods, Rottman, & Vest, 2005). The following subsections provide summaries of these XRS pre-flight calibrations and examples of those calibration results for some of the XRS units. If the calibration results are directly used by the XRS data processing system, then those initial calibrations results (i.e., Tables 3–5) are provided here for all XRS units. Some of these calibration values were revised once the instruments were on-orbit.

4.1. Responsivity Calibrations

Radiometric calibrations can be challenging for the XRS spectral range from 0.05 to 0.8 nm because of the limited number of X-ray line-sources in that range. For bright gamma sources, only the Fe^{55} has the appropriate emission within the XRS spectral range. Synchrotron radiation is also commonly used to provide X-ray radiation, but as a continuum instead of discrete emission lines. Synchrotron radiation used with a grazing incidence monochromator is commonly used to provide spectral responsivity calibrations, but only down to 5 nm for the NIST SURF facility (Canfield et al., 1989) and only down to 2 nm for the Physikalisch-Technische Bundesanstalt synchrotron calibration facility in Germany (Scholze et al., 2001).

The calibration approach for the GOES-R XRS channels was to use synchrotron radiation with multiple beam energies that produce different spectral distributions. This approach was used for the X-ray Photometer System (XPS) calibrations using SURF BL2 (Woods et al., 2008; Woods, Eparvier, et al., 2005; Woods, Rottman, & Vest, 2005). Using this same approach, XRS directly views the synchrotron radiation (without a monochromator) at multiple beam energies, and a model of the spectral response is retrieved by adjusting the thicknesses of the Be filter in the signal model until the model signal matches the measured signal. While this type of analysis can be done with a single beam energy, a more robust solution is found by using multiple beam energies, which can be especially suited for broader passbands. The SURF beam radiometric accuracy is about 1% (Arp et al., 2002), and the resulting uncertainty for XRS responsivities is about 2%. The XRS SURF calibration results as listed in Table 3 are the average responsivities from using SURF beam energies of 285, 330, 380, and 408 MeV. These XRS calibration results use known SURF beam irradiances and the Henke et al. (1993) atomic X-ray properties of Si, SiO, and Be to find optimal Be foil thickness to fit the measured photodiode signals at different beam energies. The derived Be foil thickness is systematically lower than the physically measured Be foil thickness, and this difference is directly attributed to systematic uncertainties in the atomic constants for Be. The difference between the physical thickness measurement of each Be foil filter and the modeled thickness is about 10%, which is within the uncertainties for the atomic parameters provided by Henke et al. (1993). These SURF calibration results in Table 3 include the modeled Be foil filter thickness (T) fitted with the SURF data, and the integrated responsivity

Table 4
GOES-R-Series X-Ray Sensor Diode Background Signal Model

Channel	Coefficients	GOES-16	GOES-17	GOES-18	GOES-19
D1	*a*	2.5650	2.5394	3.1430	1.8320
	b	0.1282	0.1219	0.1053	0.1575
D2	*a*	2.9886	2.5817	3.4386	2.5443
	b	0.1059	0.1364	0.1271	0.1295
A1	*a*	2.7457	2.3968	2.3378	2.5476
	b	0.1169	0.1325	0.1311	0.1195
B1	*a*	3.0812	2.7057	3.1384	2.5443
	b	0.1040	0.1163	0.9763	0.1282
A21	*a*	2.8654	2.6843	2.6713	2.7131
	b	0.1142	0.1209	0.1199	0.1176
A22	*a*	2.7559	2.6240	3.0866	2.6560
	b	0.1185	0.1160	0.1042	0.1206
A23	*a*	2.6954	2.6713	2.8001	2.7148
	b	0.1182	0.1162	0.1192	0.1184
A24	*a*	2.8058	2.6404	2.6747	2.6723
	b	0.1163	0.1190	0.1203	0.1202
B21	*a*	2.9743	2.6310	3.0622	2.9411
	b	0.1167	0.1199	0.1108	0.1174
B22	*a*	2.9303	2.8413	2.9853	2.9462
	b	0.1156	0.1132	0.1167	0.1175
B23	*a*	3.0115	2.6083	3.0793	2.9862
	b	0.1120	0.1211	0.1140	0.1173
B24	*a*	2.9272	2.9664	3.0557	3.0218
	b	0.1139	0.1110	0.1159	0.1159

Note. The A-side XRS diode background signal model coefficients (*a* and *b*) from Equation 2 are provided for the A1 and B1 channels with the larger-aperture AXUV-100 photodiodes and for A2x and B2x channels with the smaller-aperture AXUV-PS6 quadrant photodiodes, with $x = 1, 2, 3,$ or 4 for the individual photodiodes in A2 and B2. The temperature sensor used for this calibration is the XRS ASIC-1 thermistor #1.

(R, units A m^2 W^{-1}) calculated assuming a flat spectrum ($\phi(\lambda) = 1$ nm^{-1}), aperture area (A, units m^2), and modeled spectral responsivity ($\varepsilon(\lambda)$, units A/W) for the nominal passband ($\lambda 1 - \lambda 2$) using Equation 1.

$$R = \frac{A\int_0^\infty \phi(\lambda)\varepsilon(\lambda)\,d\lambda}{\int_{\lambda 1}^{\lambda 2}\phi(\lambda)\,d\lambda}(\lambda) \quad (1)$$

The use of a flat spectrum does not describe a realistic solar X-ray spectrum, but it is the method used for all previous XRS responsivity derivations. If one uses instead the APEC minimum (quiet) and maximum (active) reference spectra, then the XRS-A1 responsivities are about 3.1×10^{-5} A m^2 W^{-1} and 1.2×10^{-5} A m^2 W^{-1}, respectively. Similarly, the XRS-B1 responsivities for the APEC reference spectra are about 2.7×10^{-5} A m^2 W^{-1} and 1.4×10^{-5} A m^2 W^{-1}. We note that the responsivities derived with the APEC maximum spectrum is similar in value as the flat-spectrum responsivities, thus the quiet solar irradiance values from the standard XRS data products have significant uncertainties (factor of 2–3). The XRS model responsivities as a function of wavelength are plotted in Figure 5 for the GOES-16 XRS and provided online for all GOES-R series XRS instruments at: https://www.ncei.noaa.gov/products/goes-r-extreme-ultraviolet-xray-irradiance.

4.2. Field of View Maps

To determine the off-axis response of the filter and detector, each XRS channel was illuminated at SURF while off-pointed from its optical center using the SURF pitch-yaw gimbal table. Because the channel apertures are not directly at the gimbal center (the center of rotation), each off-point included compensating changes to X and Y of the instrument relative to SURF beam center to ensure that the channel aperture stayed at the SURF beam center. These FOV maps at SURF were done over a 9×9 grid with 0.2° step size. As expected for photometers, the XRS FOV maps have small gradients with offsets from the optical center, with these relative variations being less than 0.4% within 20 arcmin of the optical center. These pre-flight SURF FOV maps can also be verified in-orbit, as long as the solar X-ray radiation is quiescent during the FOV map experiment.

In-flight FOV maps of the XRS instruments have been obtained, and analysis of those FOV maps are compared to the pre-flight FOV maps. A concern with in-flight FOV maps is that the off-axis response due to pointing across the FOV (inflight pointing range of ±15 arcmin) is quite small and could be completely dwarfed by the variability in solar activity, even during solar-minimum conditions. For more recent times in Solar Cycle 25, the Sun has been much more active, which makes this analysis almost impossible to do. A clever way to remove this solar variability is to use the XRS signal from a different GOES satellite to remove the solar variability before examining the off-axis response due to pointing away from solar center. Shown in Figure 6 are FOV maps of GOES-18 XRS-B1 and -B2 from prelaunch calibration (top panels), and FOV maps of GOES-18 XRS-B1 and XRS-B2 from inflight test data from 28 November 2023. For the inflight data analysis (bottom panels), GOES-16 XRS data were used to remove the effects of an M9.8 solar flare that erupted during this particular FOV test. The SURF FOV map includes convoluting the solar X-ray extended disk (radius 20 arcmin) with the SURF FOV map data (SURF beam is < 2 arcmin radius) and also doing a 90° clockwise rotation to align SURF calibration axes to the GOES satellite axes.

As expected for photometers, the XRS FOV maps are relatively flat with uniformity variations being typically less than 1%. Not surprisingly, Figure 6 right-hand column maps for XRS-B2 show more of a gradient structure across the FOV, where the four diodes in XRS-B2 contribute individually to the aggregate response of XRS-B2. The FOV maps for the A-channel diodes are similar in structure and are not shown here. For the XRS-B1 map comparison (Figure 6 left-hand column maps), the SURF and flight maps show similar uniformity range of 0.05%,

Table 5
GOES-R-Series X-Ray Sensor Gain Calibration Results

Channel	Coefficients	GOES-16	GOES-17	GOES-18	GOES-19
D1	G_0	9.8840	7.6029	11.0380	11.0380
	Self-Cal Δg	−0.000005	−0.0001	−0.0006	−0.0006
D2	G_0	8.8812	9.1807	9.2789	9.2789
	Self-Cal Δg	−0.000004	−0.0002	−0.0011	−0.0011
A1	G_0	10.2556	8.8939	11.2256	9.0750
	Optical Δg	−0.0004	−0.0004	−0.0006	−0.0001
B1	G_0	9.3411	10.1505	10.1488	9.6528
	Optical Δg	−0.0005	−0.0004	−0.0010	−0.0010
A21	G_0	8.4894	9.7012	11.0279	8.5328
	Optical Δg	−0.00004	−0.0002	−0.0008	−0.0003
A22	G_0	9.1973	7.9724	11.2355	8.6812
	Optical Δg	−0.00060	0.00009	−0.0009	−0.00007
A23	G_0	9.4147	8.3157	10.8569	9.3497
	Optical Δg	−0.0004	0.0003	−0.0006	−0.0008
A24	G_0	8.8022	9.3822	9.9260	8.7742
	Optical Δg	−0.0004	−0.0004	−0.0006	−0.0006
B21	G_0	9.9193	7.0292	9.9925	9.4039
	Optical Δg	−0.0013	−0.0006	−0.0005	−0.0003
B22	G_0	9.7829	8.7920	9.6061	8.8036
	Optical Δg	−0.0012	−0.00007	−0.0005	−0.0002
B23	G_0	9.9351	8.9355	11.8292	8.6937
	Optical Δg	−0.0010	−0.0003	−0.0010	−0.0006
B24	G_0	10.2556	9.4334	10.5010	10.1904
	Optical Δg	−0.0006	−0.0004	−0.0007	−0.0007

Note. The XRS gain calibration coefficients (G_0 and Δg) from Equation 6 are listed here for the optical gain calibration, except for the Dark diodes that only have Self-Cal gain calibrations. The reference temperature, T_0, is 15°C for use in the gain equation. The photodiode channel names are D1 and D2 for the two dark channels, A1 and B1 for the larger-aperture AXUV-100 photodiodes, and A2x and B2x for the smaller-aperture AXUV-PS6 quadrant photodiodes with x = 1, 2, 3, or 4 for the individual photodiodes in A2 and B2.

but the SURF map has a slight ramp across the FOV map that is not as obvious in the flight map. For the XRS-B2 map comparison, the SURF and flight maps show similar ramp across the FOV map yaw (alpha) axis, but the flight map has larger uniformity variation (about 1.5%) in the map yaw (alpha) axis than the SURF map variation (about 0.2%). Those large differences in the XRS-B2 map variation might be the result of assuming uniform solar disk illumination for the SURF map analysis, whereas the flight FOV map can be sensitive to the position of the solar active regions, being four bright active regions on the western part of the solar disk on 28-Nov-2023. Analysis of the flight FOV maps have been challenging due to the dynamic variability of the solar X-ray irradiance during the mapping period, so we consider the SURF FOV maps as more accurate maps that could be used in data processing. Because of the excellent pointing quality of the GOES solar pointing system, FOV maps are not used in XRS data processing.

4.3. Temperature-Dependent Background Signal

The dark-signal component for all XRS diode signals was determined from data acquired during each prelaunch calibration campaign as a function of the ASIC electrometer temperature. The functional form of the model used was a two-parameter exponential, where the two unknown parameters were allowed to vary to minimize χ^2 of the fit:

$$S_D = e^{(a+bT)} \tag{2}$$

Here, T is the ASIC temperature in ℃, and a and b are the two unknown parameters. The tests for a given day were done at a predetermined temperature set-point inside a thermally controlled, evacuated tank that housed the EXIS instrument, which was mounted on a movable pitch-yaw gimbal table. Model-fit results for flight-model 4 (GOES-19) are shown in Figure 7, and the background signal fit parameters for all GOES-R-series XRS units are listed in Table 4. The background signal dependence on temperature is very similar for the different photodiodes and ASIC electrometers on all four XRS units. The on-orbit temperature of XRS has very little variation, so the prelaunch background signal model with temperature is used in the XRS data processing. However, the on-orbit background (dark) measurements do indicate a trend with time for all XRS channels, and those on-orbit measurements provide an offset for the prelaunch-derived background signal model with temperature.

4.4. Temperature-Dependent Gain

The XRS detector gain (fC/DN) changes slowly with temperature, due to temperature-dependent variations in the electrical properties of the circuitry (primarily the resistance and capacitance of the electrometer and photodiode). Each ASIC electrometer has a self-calibration (Self-Cal) circuit which injects a known current (ramped at 4 levels) into each channel, from which the absolute gain can be determined by comparing the measured signal with the known current input. By running the Self-Cal ramp at various temperatures, the gain temperature dependence can be determined for each channel. The Self-Cal ramps can be performed in any laboratory setting and for in-flight gain checks. The temperature dependence for a channel can also be determined optically, by illuminating the channel with a constant-intensity beam and observing how the relative signal changes with temperature. Both the Self-Cal ramp and optical methods were performed at SURF, and those results are used to determine the gain as a linear function of temperature as given by Equation 3.

$$G(T) = G_0[1 + \Delta g(T - T_0)] \tag{3}$$

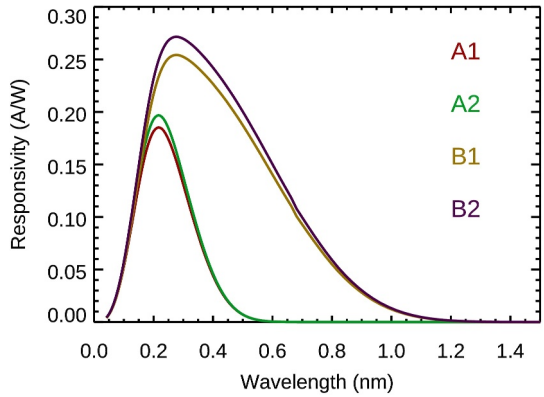

Figure 5. The GOES-16 X-Ray Sensor (XRS) modeled responsivities, as based on Synchrotron Ultraviolet Radiation Facility calibrations, are plotted as a function of wavelength. These spectral responsivities are convolved with the reference spectrum over the XRS bands (Equation 1), and those passband responsitivites are provided in Table 3 and used in XRS data processing.

An example of the XRS gain calibrations is shown for the GOES-18 XRS instrument in Figure 8. The slope of this temperature dependence (Δg) ranges from -1×10^{-3} per °C to 1×10^{-3} per °C for the different XRS channels. Therefore, gain changes over 10°C can be as large as 1%, and so the gain corrections are important to include in data processing. The optical gain results, which are considered more accurate than the Self-Cal method, are used for science data processing. There are slight differences between the optical gain and Self-Cal gain results, but within the required 2% uncertainty. The XRS FM4 optical gain calibrations are illustrated in Figure 8, and the gain calibrations are listed in Table 5 for all four XRS units. The in-flight Self-Cal gains are executed quarterly to monitor the ASIC electrometer performance relative to the pre-flight Self-Cal gain results. These in-flight gain calibrations have not revealed any significant changes over time. As mentioned earlier, the on-orbit temperature variation is small, so the prelaunch gain model with temperature is the calibration set used in the XRS data processing.

4.5. Sensor Linearity Validation

Laboratory measurements of the XRS electrometer have shown that its response (output DN per input fA) is extremely linear across its full dynamic range, and laboratory measurements of the IRD Si photodiodes have shown them to be very linear to higher than 1 μA. The linearity of response of the entire detector, photodiode and electrometer, is verified at SURF by illuminating each channel with varying beam intensity and comparing the measured beam current (BC)-normalized signal at each BC. Because the beam intensity is directly proportional to BC, the BC-normalized signal should ideally remain completely flat for a linear response. For each channel, the BC was varied such that measurements were obtained at multiple signal levels from background level to electrometer saturation level. An example of the linearity validation is shown in Figure 9 for the GOES-17 XRS-B2 channel. No non-linear effects were noted in any of the SURF linearity calibrations for the XRS channels, so XRS data processing do not require any non-linearity corrections.

4.6. Early Validation With Sounding Rocket Flights of Prototype XRS

An engineering model (EM) of the new XRS for the GOES-R series was calibrated at NIST SURF using this multiple beam energy technique and then flown on a NASA sounding rocket flight on 28 October 2006. This XRS rocket unit is identical to the XRS flight design, except that the extra Al-W shielding and magnetic sweep assembly are not flown on the rocket. From this flight, the rocket XRS-A measured a solar irradiance of 2.1×10^{-9} W m^{-2} versus the GOES-12 XRS-A result of 2.0×10^{-9} W m^{-2}, and the rocket XRS-B result is 6.8×10^{-8} W m^{-2} versus the GOES-12 XRS-B result of 6.2×10^{-8} W m^{-2}. These rocket irradiance values are corrected to the appropriate XRS-A and XRS-B nominal passbands, and the GOES-12 XRS values are scaled up to irradiance values using the standard GOES-12 calibration factors of 1.16 and 1.43 for XRS-A and XRS-B, respectively. This comparison indicates that the new XRS results agree with the original GOES XRS to better than 10%.

4.7. XRS Irradiance Uncertainty Based on the Pre-Flight Calibrations

The EXIS PORD specifies that the XRS irradiance accuracy must be better than 20%. This section discusses the many factors that are included into the XRS irradiance accuracy (total uncertainty) budget. One important assessment for the in-flight XRS measurements and related comparisons is to calculate the statistical uncertainty, σ_E/E, for a computed irradiance, E. To begin with, the photodiode current, C, is defined to be:

$$C = \frac{G(S - S_0)}{\Delta t} \tag{4}$$

Here, S is the raw in-flight signal in units of DN, S_o is the model dark signal at a given detector temperature (T) in units of DN, G is the detector gain and is also temperature dependent, and Δt is the integration time. By propagation of errors, the following relationship for σ_c is:

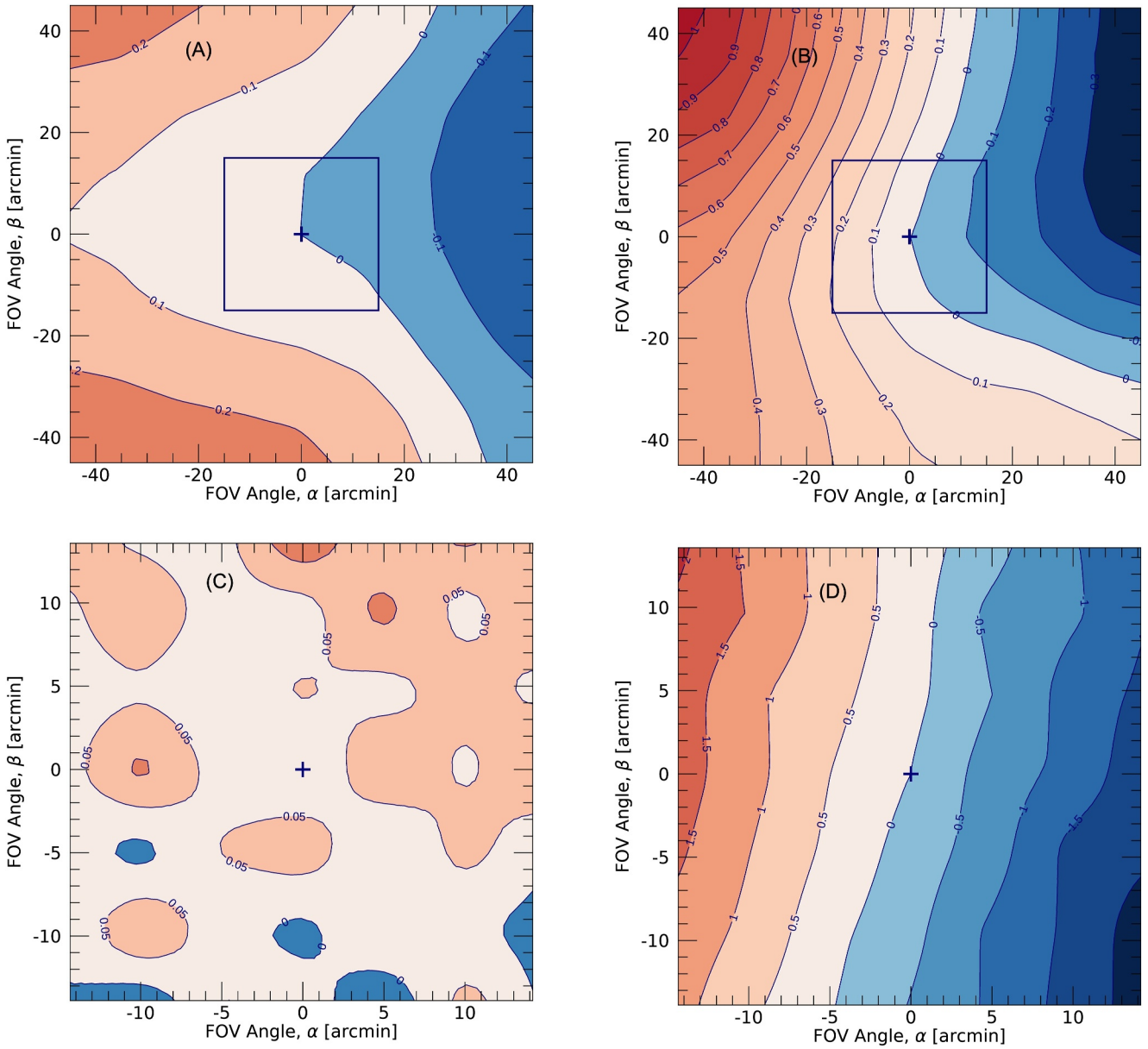

Figure 6. Field of view (FOV) maps for GOES-18 XRS-B1 are in panels A and C, and FOV maps for GOES-18 XRS-B2 are in panels B and D. Top panels are maps from prelaunch calibration, and the bottom panels were from an inflight FOV map obtained on 28 November 2023. The bottom FOV maps are over ±15 arcmin (0.25°), and the flight map range of ±15 arcmin is represented as a solid-black box in the top FOV maps that are over ±45 arcmin (0.75°).

$$\sigma_C = C\left[\left(\frac{\sigma_G}{G}\right)^2 + \left(\frac{\sigma_S}{S-S_0}\right)^2 + \left(\frac{\sigma_{S_0}}{S-S_0}\right)^2 + \left(\frac{\sigma_{\Delta t}}{\Delta t}\right)^2\right]^{1/2} \quad (5)$$

The uncertainties σ_G and σ_{S_0} are calculated from separate analyses of pre-flight calibration data, and $\sigma_{\Delta t} = 10$ ms. The uncertainty σ_S is constructed dynamically as a function of the in-flight signal size during this analysis. To convert photodiode current into irradiance, the photodiode current (C, units A) is divided by the photodiode responsivity (R), that is, $E = C/R$, to yield the irradiance (E, units W m^{-2}). The uncertainty, σ_E, is derived by error propagation as:

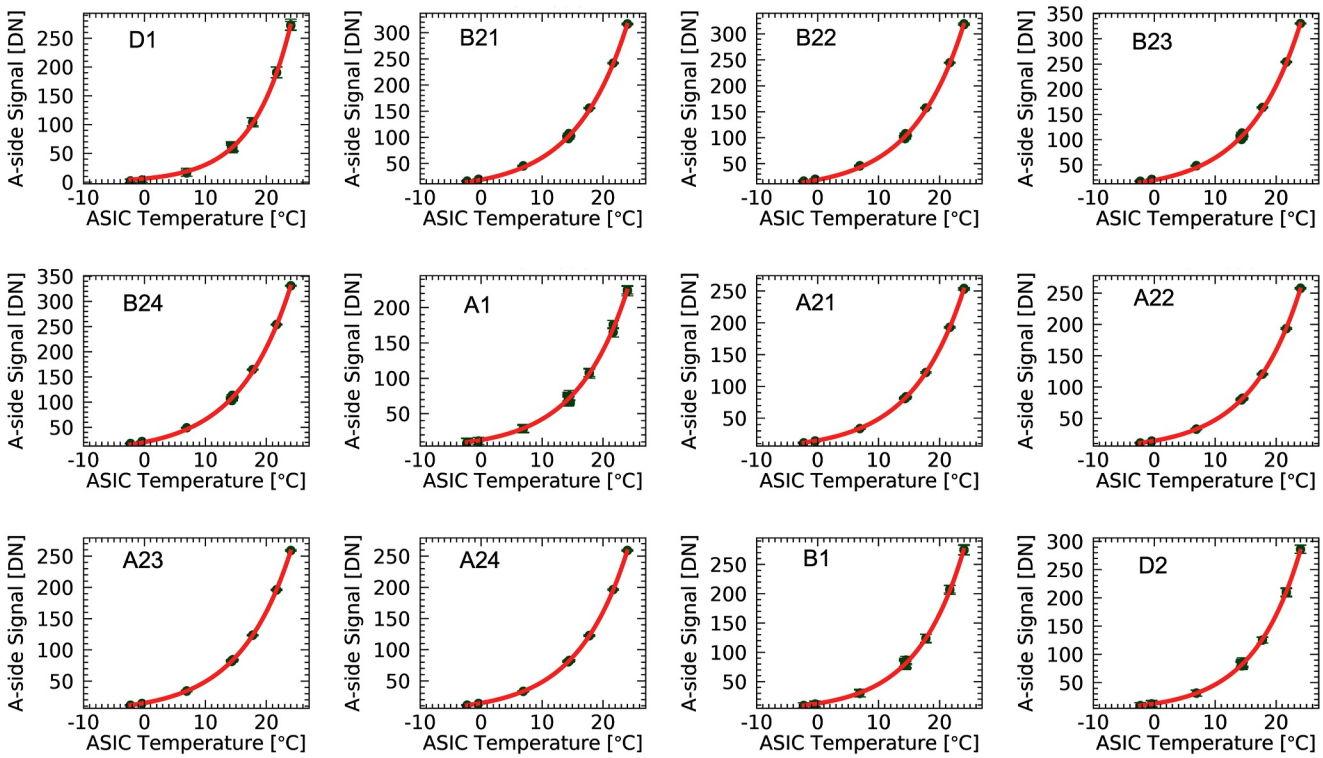

Figure 7. Model-fit results for all X-Ray Sensor (XRS) diodes background signal for the GOES-U (GOES-19) XRS unit. These results are typical for the other XRS flight models (FM). The Dark diodes are D1 and D2. AXUV-100 diodes are used for XRS A1 and B1. AXUV-PS6 quadrant diodes are used for A2 and B2, with labels for its four diodes as X21, X22, X23, and X24 (where X is A or B).

$$\sigma_E = E\left[\left(\frac{\sigma_C}{C}\right)^2 + \left(\frac{\sigma_R}{R}\right)^2\right]^{1/2} \tag{6}$$

The calculation of σ_R uses pre-flight calibration data, exclusively, where:

$$R = \frac{G(S - S_0)}{E_{\text{SURF}} \cdot I \cdot \Delta t} \tag{7}$$

Here, I is the SURF BC in units of mA. Applying error propagation, we have:

$$\sigma_R = R\left[\left(\frac{\sigma_G}{G}\right)^2 + \left(\frac{\sigma_S}{S - S_0}\right)^2 + \left(\frac{\sigma_{S_0}}{S - S_0}\right)^2 + \left(\frac{\sigma_{E_{\text{SURF}}}}{E_{\text{SURF}}}\right)^2 + \left(\frac{\sigma_I}{I}\right)^2 + \left(\frac{\sigma_{\Delta t}}{\Delta t}\right)^2\right]^{1/2} \tag{8}$$

The relative uncertainty in the gain, σ_G, is 0.09%. The relative uncertainties in the signal and background signal, σ_S and σ_{S_0}, are less than 0.2% for SURF measurements. The relative uncertainty in the SURF beam irradiance, $\sigma_{E_{\text{SURF}}}$, for the X-ray wavelengths is 1.5%. The relative uncertainty in the BC, σ_I, is 1.3%. The relative uncertainty in the integration time, $\sigma_{\Delta t}$, is 0.01%. So the typical relative uncertainty for the SURF-based responsivity for XRS is 2.0%.

Shown in the top panel of Figure 10, is the relative statistical uncertainty, σ_E/E, plotted against irradiance for GOES-18 XRS-A1 and -B1 on 3 May 2022, and in the bottom panel, XRS-B1 is shown for GOES-16, -17, and −18. The XRS irradiance uncertainty (accuracy) is less than 3% for solar measurements above a C1-flare level (1×10^{-6} W m^{-2}), and this is significantly smaller than the XRS PORD requirement of 20%. The irradiance uncertainty is larger for smaller A-class and B-class levels, more so for XRS-A band.

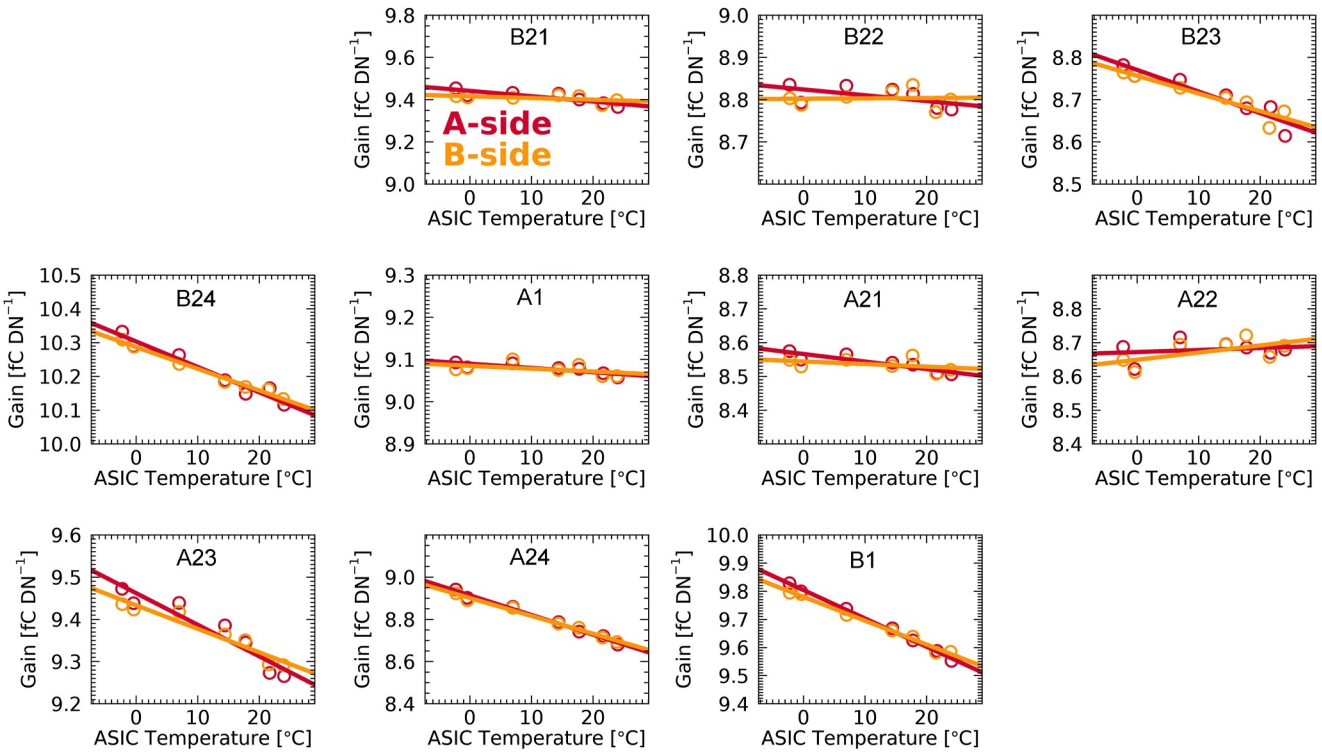

Figure 8. The GOES-18 XRS optical gain versus temperature for the EXIS A-side and B-side electronics. The red and orange lines are linear fits to the gains for the Synchrotron Ultraviolet Radiation Facility optical gain calibrations for the A-side and B-side, respectively. The dark diode gains are not shown because their apertures are blocked off so they can not see light. The diode names used in this figure are the same as defined for Figure 7.

It is interesting to note that the three traces shown in the bottom panel of Figure 10 are similar in magnitude and shape for the in-flight XRS-B1 sensors. The similar behavior of these three traces can mostly be attributed to a robust pre-flight calibration campaign for each EXIS flight instrument, as the XRS design and construction were identical. Even though each instrument is a replication of another, deviations in some components (e.g., photodiode noise levels) can drive differences to the level that is observed in the statistical uncertainty traces in the bottom panel of Figure 10. The SURF facility at NIST provided a very stable and reproducible point-source photon beam that was used extensively on each SURF calibration trip to characterize the instrument performance

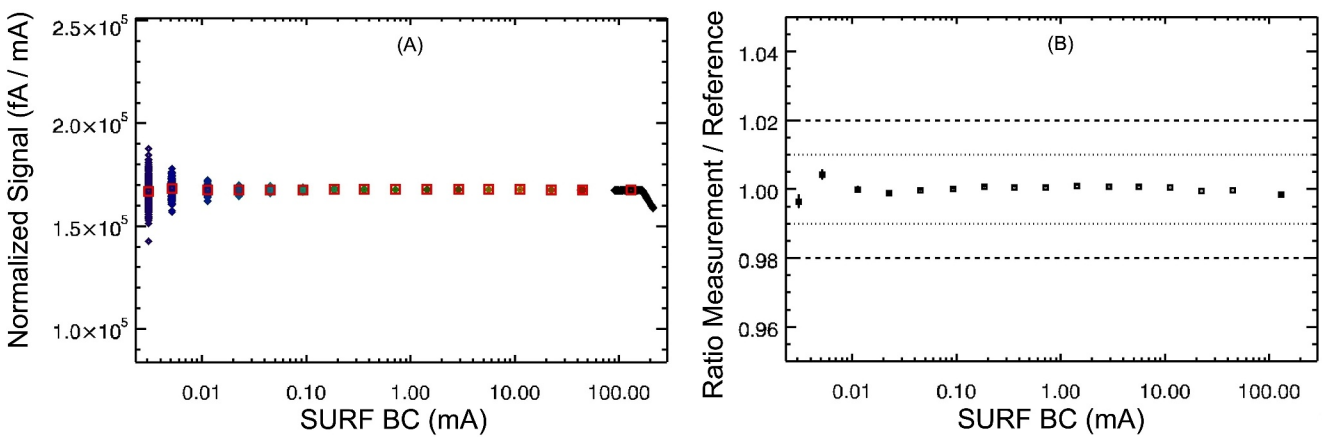

Figure 9. The GOES-17 XRS-B2 linearity calibration at Synchrotron Ultraviolet Radiation Facility (SURF). (left) Beam current (BC)-normalized signal (summed over all quadrants) versus SURF BC reveals a flat level independent of SURF BC. Blue diamonds represent individual data points, and red squares show the average values for measurements taken at different BC levels. The rollover at high BC is due to electrometer saturation. (right) Deviations from the mean normalized signal is also very flat, with ±1% dotted lines and ±2% dashed lines shown for reference.

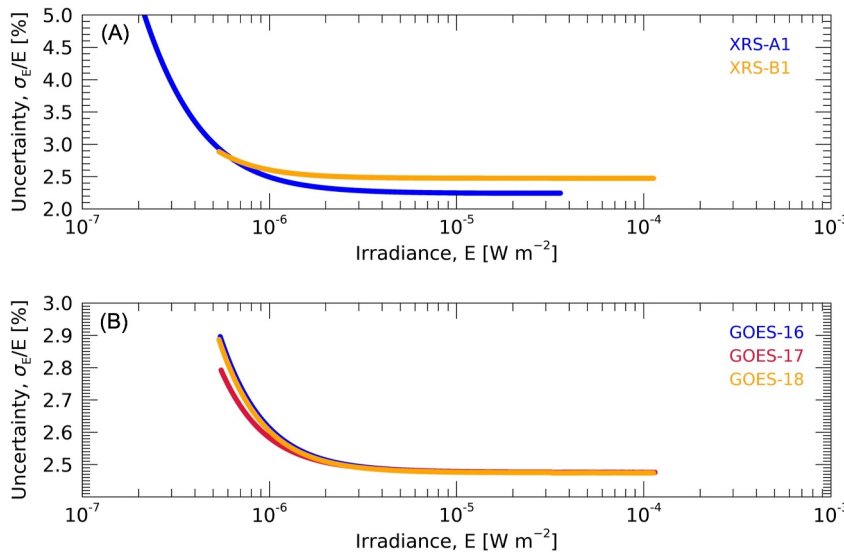

Figure 10. The relative statistical uncertainty, σ_E/E, plotted in the top panel as a function of irradiance (in W m^{-2}) for both XRS-A1 and -B1 aboard GOES-18. Bottom panel shows the statistical uncertainties for XRS-B1 on GOES-16, -17, and -18. These results are for in-flight solar measurements on 3 May 2022 (day of year 123).

before launch. Because the statistical uncertainty in the irradiance is heavily dependent on the pre-flight calibration of XRS, the likeness in the traces is a testament to the rigorous calibration testing that was performed on each SURF trip. The estimated irradiance statistical uncertainties at C-1, M-1, and X-1 class flare levels are 2.60%, 2.48%, and 2.47%, respectively.

The on-orbit, electron-background contribution to the irradiance uncertainty is not fully incorporated in the above irradiance accuracy discussion because the electron-background contribution is highly dependent on the level of the energetic electron storm and also on the solar signal level. For example, this electron-background contribution is larger (up to 100% during the largest electron flux levels) near solar cycle minimum conditions when the solar X-ray signal is small, and this contribution is significantly smaller (<1%) for M and X class flares when the solar signal is large. The new XRS includes dark photodiodes so that on-orbit measurements of the background signal variations are obtained. These dark photodiodes have similar shielding as the solar-active photodiodes, but these dark photodiodes do not have any solar-viewing apertures. In addition to the dark photodiode measurements, the Space Environment In-Situ Suite (SEISS) aboard the GOES satellites directly measures the electron flux as a function of electron energy, and these SEISS electron flux measurements are used to further correct electron-background signal for XRS minimum channels. Based on the root-mean-squared (rms) of the pre-flight calibration uncertainties and this extra electron-background correction uncertainty, the estimated on-orbit accuracy for XRS irradiance is 10% for C1, 3.2% for M1, and 3.0% for X1 levels.

5. XRS Post-Launch Tests

The in-flight performance characterization period for each GOES-R Series satellite begins approximately 30 days after launch. For EXIS, the suite of tests for all sensors usually takes about 3 months to complete. During this post-launch test (PLT) phase, some of these tests are performed to identify any changes that might have occurred during the launch process or from in-flight conditions. Most calibration parameters are determined during pre-flight calibration, and remain unchanged post launch; however, shifts in pointing, photodiode dark signals, or electrometer gains can be measured and used to update scientific data processing look-up tables, or for monitoring purposes. In addition, comparison of the concurrent solar signals from XRS channels are used to validate pre-flight calibration results and to develop new functions of the background signals that are caused by the energetic electrons in orbit. A couple of those PLT results are presented in this XRS Paper-1, and additional in-flight results are presented in the XRS Paper-2 (Machol et al., 2024).

As one example of PLT validation, the in-flight solar signals are compared to the range of estimated solar signals as listed in Table 2, which are based on XRS responsivities (Figures 2 and 5) and the APEC solar reference spectra

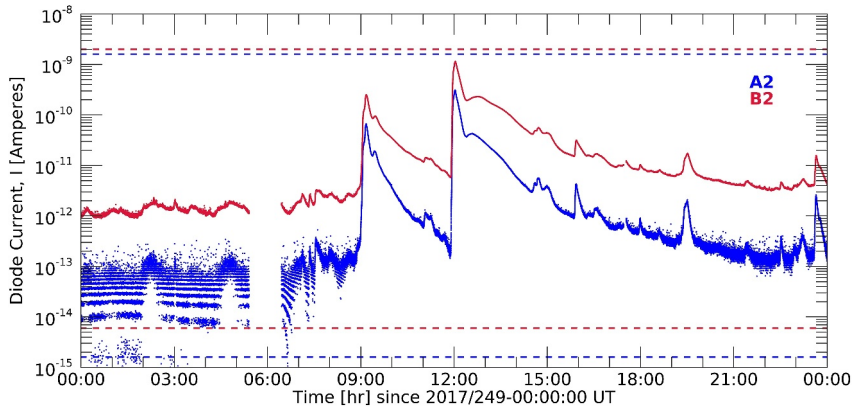

Figure 11. Example of in-flight X-Ray Sensor (XRS) signals for GOES-16 XRS A2 and B2 on day 2017/249 (6 September 2017) when there was a large X10 flare near 12 UT. These XRS signals are first corrected for the background signal, which is a bigger effect during non-flaring times for A2 than B2. The estimated signals for the Astrophysical Plasma Emission Code solar minimum and maximum reference spectra are the horizontal dashed lines (blue for A2 and red for B2).

(Figure 3). The GOES-16 XRS A2 and B2 signals, after being corrected for background signal, are shown in Figure 11 for day 2017/249 (6 September 2017) when there was a X10 flare that saturated the XRS-B1 channel. These in-flight XRS A2 and B2 measurements are within the expected solar signals calculated with the APEC solar minimum and maximum reference spectra (Figure 3); those expected solar signals are shown in this figure as the dashed horizontal lines. With the A2 and B2 channels being the flare channels, it is important that there is significant margin between the measured signal during the X10 flare near 12 UT and the estimated signal for the APEC maximum spectrum (upper lines). For this comparison, the XRS-B2 non-flaring signal is also high quality and well above the estimated signal for the APEC minimum spectrum (lower lines). The XRS-A2 non-flaring signal is noisier and the discrete data numbers (DN) from the XRS electrometer are obvious in the 0–8 UT range. In other words, the XRS-A2 signal is very close to the A2 background level in the 0–8 UT range, and the A2 signal minus its background level in that range shows up as horizontal bands at the 1 DN, 2 DN, 3 DN, etc. levels above the background value. We note that the less noisy data from XRS A1 and B1 channels, with their much larger aperture areas, are used for the XRS data products during non-flaring times.

While laboratory tests confirmed the performance for the XRS magnet assembly for on-axis electrons, the XRS flight data show a larger background signal for the new XRS units than anticipated. From the in-flight results as provided in the XRS Paper-2 (Machol et al., 2024), this generation of XRS still observes high-energy electrons, and these impact the in-flight background signal and thus the solar X-ray measurements at the lowest irradiance levels (A-class and low B-class flare levels). Further analysis of the XRS mechanical design indicated that the enhanced background was likely due to off-axis electrons interacting with the baffle assembly and producing bremsstrahlung X-ray radiation in the optical cavity. The energetic protons do not normally elevate the photodiode background signal, except for the largest particle storms, because the Al-W shielding protects XRS from most of the off-axis protons, and for along-the-optical axis, the magnet assembly has little effect on the high energy protons, but those energetic protons are mostly transmitted through the Be filters and Si photodiodes.

To test the aforementioned enhanced-background hypothesis, a full, flight-like XRS assembly was brought to the electron-beam (e-beam) facility at Goddard Space Flight Center (GSFC) in spring 2019 to test different baffle assemblies to better understand the potential adverse effects from electrons entering the XRS-A1 and -B1 apertures. Three XRS shielding configurations were tested:

1. Configuration 1: Original flight baffles
2. Configuration 2: Additional tungsten (W) baffles, tucked behind the Al flight baffles to help suppress the in-band characteristic X-ray contribution from W.
3. Configuration 3: Replace the W flight baffles with ones constructed from Al.

Those test results suggested that the new baffle arrangements did not improve the background signal in XRS; therefore, no alterations were made to the XRS flight models in storage (awaiting launch).

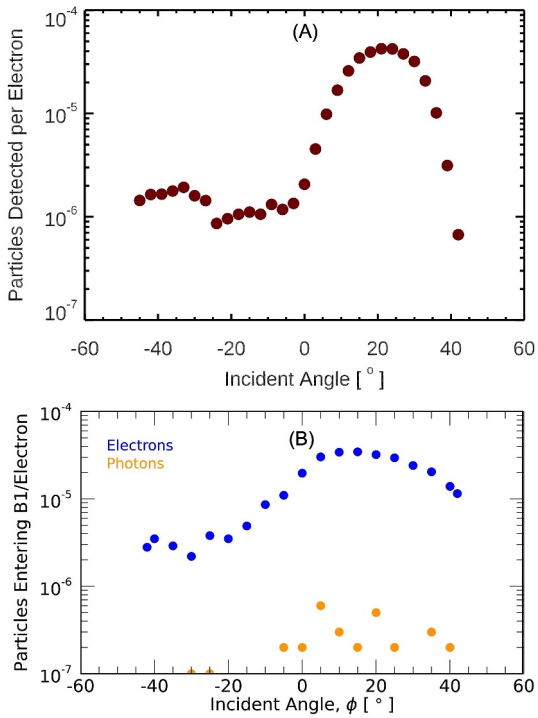

Figure 12. GSFC e-beam facility results with an incident electron beam energy of 300 keV (top panel) and Geant4 model results (bottom panel) for an identical experimental configuration and conditions show similar incidence-angle dependence for the XRS magnet assembly. The Geant4 model also indicates that electrons dominate the background much more than the electron-excited photons.

To better understand the e-beam results, the full XRS e-beam experiment was modeled using Geant4. This modeling exercise included the preparation of the following inputs for the Geant4 model.

1. A fully rendered computer-automated design (CAD) volume representation of the full XRS instrument was implemented.
2. A 3-D Opera (Dassault Systemes, Simulia Product Line: Opera (www.3ds.com)) model computation of the internal magnetic field of the configured Sm-Co bar magnets in the magnet assembly was used.
3. We specified all electron beam characteristics (e.g., beam-spot size, Gaussian energy profile, and angle-of-incidence of beam) as input for the Geant4 model.

The Geant4 model also differentiates between photons and electrons that made it to the diode substrate. As shown in Figure 12, the results from an e-beam test with an incident electron beam energy of 300 keV, at a particular orientation of XRS, are compared with the Geant4 simulation results of an identical experimental configuration and electron beam conditions. The incident angle is the incoming electron beam angle into the XRS magnet assembly front baffle aperture. Both Figure 12 panels show enhanced signal for large incident positive beam angles, while falling off toward negative angles. The asymmetry is due mostly to the differences in the magnet and shielding configuration within the XRS magnet assembly. Furthermore, the model results (bottom panel) shows that electrons are the dominant particle entering the diode compared to photons produced upstream of the detector. It should be noted that the Geant4 simulation does not have a detailed depiction of the physics of the Si detector response; in particular, the Geant4 simulation does not account for the transmission of high-energy particles through the Si detector. Consequently, the Geant4 simulation result is much larger (about a factor of two) than the measured signal for a similar electron beam input.

The pre-flight tests at GSFC with energetic electron beams do indicate higher detection of the high-energy electrons by the XRS detectors than expected. This Geant4 model was an interesting exercise to study a full simulation of this e-beam experiment, and this type modeling could provide a useful tool for improving future XRS designs at geostationary orbits. In particular, improvements for both the magnetic sweeping assembly and the shielding near the magnetic sweeping assembly could be considered for future XRS instruments.

6. Summary

The next-generation XRS for the GOES-R series of satellites is extending the long-term time series of the solar X-ray irradiance obtained by previous GOES missions. Furthermore, the GOES-R XRS instrument has improved performance due to using more sensitive Si photodiodes instead of ionization cells, new low-noise ASIC electrometers to improve measurement precision, multiple photodiodes for both XRS-A and XRS-B channels to enhance the full measurement range, and dark-channel photodiodes for monitoring the high-energy electron background. A new capability for the new XRS is providing flare location information by using quadrant photodiodes. Machol et al. (2024) discusses this new flare-location capability for XRS, along with many details about the in-flight performance of the XRS instruments aboard the GOES-16, 17, and 18 satellites. These XRS instruments have all had very steady performance for more than 7 years of operations, and we expect them to continue the temporal record of solar X-ray monitoring by NOAA for many years to come.

Data Availability Statement

Links to the GOES XRS science-quality and operational XRS data products, XRS Data User's Guide, and other associated documentation can be found at https://www.ncei.noaa.gov/products/goes-r-extreme-ultraviolet-xray-irradiance.

Acknowledgments
We are very grateful for the dedicated team of engineers, scientists, and managers at the Laboratory for Atmospheric and Space Physics (LASP) at the University of Colorado for the development of these next-generation GOES-R XRS instruments. We are also thankful for the NOAA and NASA-GSFC leadership and guidance for the GOES-R program and the GOES-R spacecraft team at Lockheed-Martin. We also thank the two reviewers for their many useful comments to help improve this manuscript. This research is supported by NASA contract NNG07HW00C at the University of Colorado. J. Machol was supported by NOAA Cooperative Agreements NA22OAR4320151 and NA17OAR4320101.

References

Aalamia, D., & Jones, A. (2009). A low-noise ASIC electrometer for precision low-current measurements. *Proceedings of SPIE*, *7438*, 743816. https://doi.org/10.1117/12.824364

Agostinelli, S., Allison, J., Amako, K., Apostolakis, J., Araujo, H., Arce, P., et al. (2003). Geant4 - A simulation toolkit. *Nuclear Instruments and Methods in Physics Research Section A: Accelerators, Spectrometers, Detectors and Associated Equipment*, *506*(3), 250–303. https://doi.org/10.1016/S0168-9002(03)01368-8

Arp, U., Clark, C. W., Farrell, A. P., Fein, E., Furst, M. L., & Hagley, E. W. (2002). Synchrotron ultraviolet radiation facility SURF III. *Review of Scientific Instruments*, *73*(3), 1674–1676. https://doi.org/10.1063/1.1445833

Bailey, S. M., Woods, T. N., Barth, C. A., Solomon, S. C., Canfield, L. R., & Korde, R. (2000). Measurements of the solar soft X-ray irradiance from the Student Nitric Oxide Explorer: First analysis and underflight calibrations. *Journal of Geophysical Research*, *105*(A12), 27179–27193. https://doi.org/10.1029/2000JA000188

Canfield, L. R., Kerner, J., & Korde, R. (1989). Stability and quantum efficiency performance of silicon photodiode detectors in the far ultraviolet. *Applied Optics*, *28*(18), 3940. https://doi.org/10.1364/AO.28.003940

Chamberlin, P. C., Woods, T. N., Eparvier, F. G., Jones, A. R., & Fennelly, J. A. (2009). Next generation x-ray sensor (XRS) for the NOAA GOES-R satellite series. *Proceedings of SPIE*, *7438*, 743802. https://doi.org/10.1117/12.826807

Garcia, H. A. (1994). Temperature and emission measure from GOES soft X-Ray measurements. *Solar Physics*, *154*(2), 275–308. https://doi.org/10.1007/BF00681100

Henke, B. L., Gullikson, E. M., & Davis, J. C. (1993). X-ray interactions: Photoabsorption, scattering, transmission, and reflection at E = 50–30,0000 eV, Z = 1–92. *Atomic Data and Nuclear Data Tables*, *54*, 181. https://doi.org/10.1006/adnd.1993.1013

Hill, S., Pizzo, V., Reinard, A., Biesecker, D., & Viereck, R. (2005). The NOAA GOES X-ray calibration program. *Proceedings of SPIE*, *5901*, 59010E. https://doi.org/10.1117/12.619109

Hudson, H. (2011). Global properties of solar flares. *Space Science Reviews*, *158*(1), 5–41. https://doi.org/10.1007/s11214-010-9721-4

Hudson, H., Cliver, E., White, S., Machol, J., Peck, C., Tolbert, K., et al. (2024). The Greatest GOES Soft X-ray Flares: Saturation and Recalibration over Two Hale Cycles. *Solar Physics*, *299*(3), 39. https://doi.org/10.1007/s11207-024-02287-x

Korde, R., & Canfield, L. R. (1989). Silicon photodiodes with stable near theoretical quantum efficiency in the soft X-ray region. *Proceedings of SPIE*, *1140*, 126. https://doi.org/10.1117/12.961812

Lei, F., Truscott, P. R., Dyer, C. S., Quaghebeur, B., Heynderickx, D., Nieminen, P., et al. (2002). MULASSIS: A Geant4-based multilayered shielding simulation tool. *IEEE Transactions on Nuclear Science*, *49*(6), 2788–2793. https://doi.org/10.1109/TNS.2002.805351

Machol, J., Codrescu, S., Peck, C. L., Mothersbaugh, III, J. F., Negus, J., Woodraska, D. L., et al. (2024). GOES-R Series X-Ray Sensor (XRS): 2. On-orbit measurements and calibrations. *Journal of Geophysical Research: Space Physics*. to be submitted. (XRS Paper-2 reference).

Neupert, W. M. (2011). Intercalibration of solar soft X-ray broad band measurements from SOLRAD 90 through GOES-12. *Solar Physics*, *272*(2), 319–335. https://doi.org/10.1007/s11207-011-9825-3

Scholze, F., Thornagel, R., & Ulm, G. (2001). Calibration of energy-dispersive X-ray detectors at BESSY I and BESSY II. *Metrologia*, *38*(5), 391–395. https://doi.org/10.1088/0026-1394/38/5/4

Smith, R. K., Brickhouse, N. S., Liedahl, D. A., & Raymond, J. C. (2001). Collisional plasma models with APEC/APED: Emission-line diagnostics of hydrogen-like and helium-like ions. *The Astrophysical Journal*, *556*(2), L91–L95. https://doi.org/10.1086/322992

Wang, Y., & Zhang, J. (2007). A comparative study between eruptive X-class flares associated with coronal mass ejections and confined X-class flares. *The Astrophysical Journal*, *665*(2), 1428–1438. https://doi.org/10.1086/519765

White, S. M., Thomas, R. J., & Schwartz, R. A. (2005). Updated expressions for determining temperatures and emission measures from GOES soft X-ray measurements. *Solar Physics*, *227*(2), 231–248. https://doi.org/10.1007/s11207-005-2445-z

Woods, T. N., Caspi, A., Chamberlin, P. C., Jones, A., Kohnert, R., Mason, J. P., et al. (2017). New solar irradiance measurements from the Miniature X-ray Solar Spectrometer CubeSat. *The Astrophysical Journal*, *835*(2), 122. https://doi.org/10.3847/1538-4357/835/2/122

Woods, T. N., Chamberlin, P. C., Peterson, W. K., Meier, R. R., Richards, P. G., Strickland, D. J., et al. (2008). XUV Photometer System (XPS): Improved irradiance algorithm using CHIANTI spectral models. *Solar Physics*, *249*, 235. https://doi.org/10.1007/s11207-008-9196-6

Woods, T. N., Eparvier, F. G., Bailey, S. M., Chamberlin, P. C., Lean, J., Rottman, G. J., et al. (2005). The Solar EUV Experiment (SEE): Mission overview and first results. *Journal of Geophysical Research*, *110*(A1), A01312. https://doi.org/10.1029/2004JA010765

Woods, T. N., Hock, R., Eparvier, F., Jones, A. R., Chamberlin, P. C., Klimchuk, J. A., et al. (2011). New solar extreme ultraviolet irradiance observations during flares. *The Astrophysical Journal*, *739*(2), 59. https://doi.org/10.1088/0004-637X/739/2/59

Woods, T. N., Rottman, G., & Vest, R. (2005). XUV Photometer System (XPS): Overview and calibrations. *Solar Physics*, *230*(1–2), 345–374. https://doi.org/10.1007/s11207-005-4119-2

Woods, T. N., Schwab, B., Sewell, R., Telikicherla-Kandala, A. K., Mason, J. P., Caspi, A., et al. (2023). First results for solar soft X-ray irradiance measurements from the third generation Miniature X-Ray Solar Spectrometer. *The Astrophysical Journal*, *956*(2), 94. https://doi.org/10.3847/1538-4357/acef13